Supplementary information for

Dual-Function Surface Hydrogen Bonds Enable Robust O_2 Activation for Deep Photocatalytic Toluene Oxidation

Hao Li,[†,‡] *Fuze Jiang,*[†,‡] *Sarka Drdova,*[†,‡] *Huan Shang,*[§] *Lizhi Zhang*[§] *and Jing Wang*[*,†,‡]

[†]Institute of Environmental Engineering, ETH Zürich, Zürich 8093, Switzerland

[‡]Laboratory for Advanced Analytical Technologies, Empa, Swiss Federal Laboratories for Materials Science and Technology, Dübendorf 8600, Switzerland

[§]Key Laboratory of Pesticide & Chemical Biology of Ministry of Education, Institute of Applied & Environmental Chemistry, College of Chemistry, Central China Normal University, Wuhan 430079, P. R. China

25 pages, 20 figures, 2 tables

CONTENTS

1. Characterization Methods

The powder X-ray diffraction (XRD) patterns of the samples were recorded on a Bruker D8 Advance diffractometer with monochromatized Cu Kα radiation (λ = 0.15418 nm). The morphology of the samples was observed with a JEOL 6700-F field-emission scanning electron microscope (SEM) and elemental mappings were collected by it, too. The transmission electron microscopy (TEM) and selected area electron diffraction (SAED) images were obtained by JEOL JSM-2010. Chemical compositions and states were analyzed using X-ray photoelectron spectroscopy (XPS) (Thermo Scientific ESCLAB 250Xi). All binding energies were referenced to the C 1s peak (284.6 eV) arising from the adventitious carbon. UV-visible diffused reflectance spectra of the samples were obtained for the dry-pressed film samples using a UV-visible spectrophotometer (UV-2550, Shimadzu, Japan) with $BaSO_4$ as the reflectance standard. Electron paramagnetic resonance (EPR) spectra were conducted on a Bruker EMX EPR Spectrometer (Billerica, MA). FTIR spectra was recorded by Nicolet iS50FT-IR spectrometer (Thermo, USA) with a designed reaction cell. The system for steady-state and transient surface photovoltage (SPV) measurements included a source of monochromatic light, a lock-in amplifier (SR830-DSP) with a light chopper (SR540), a photovoltaic cell, and a computer. A 500-W xenon lamp (CHFXQ500 W, Global Xenon Lamp Power) in conjunction with a double-prism monochromator (Zolix SBP500) provided monochromatic light as the light source. The samples were examined without further treatment during the SPV measurements, and the contact between the sample and the ITO electrode was nonohmic. Steady-state and time-resolved photoluminescence (PL) measurements were carried out on an FLS900 fluorometer (Edinburgh Instruments). O_2 temperature-programmed desorption experiments (O_2-TPD) were recorded on AutoChem II 2920 (Micromeritics, USA) using a TCD detector. Desorbed O_2 under UV light was monitored by a mass spectrometer (Trace 1300-ISQ, Thermo). Zeta-potential of the photocatalysts in water was measured by a Malvern zeta analyzer (Nano-ZS 90, MalvernInstrument, UK). The intermediates associated with toluene oxidation were analyzed by a gas chromatography–mass spectrometry (GC-MS, Trace 1300-ISQ, Thermo) with a TG-5MS column (injector temperature = 280 °C, helium flow = 1.0 mL/min) and liquid chromatography-mass spectrometry (LC–MS, TSQ Quantum Access MAX, Thermo) in positive ESI mode with a Hypersil ODS-C18 column. Libraries NIST MS Search was applied to identify the intermediates.

2. Supplementary Figures and Discussions

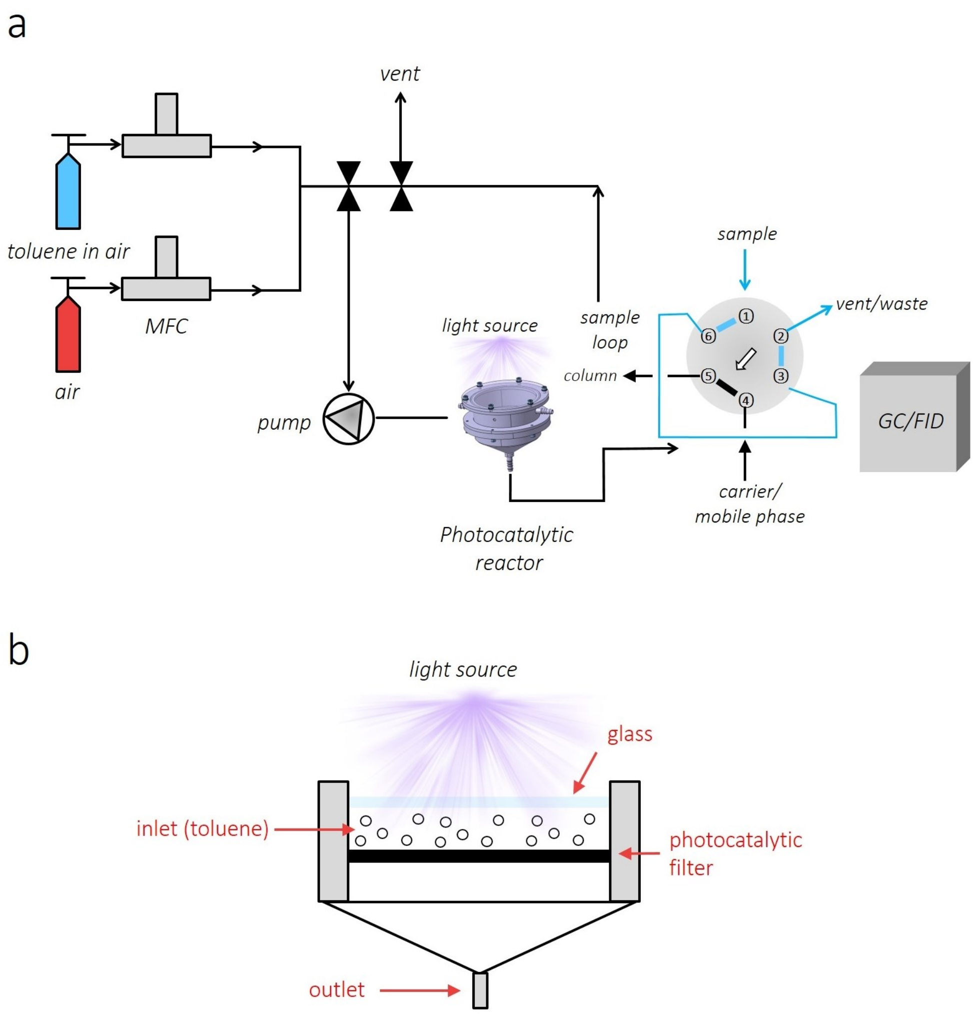

Figure S1. Schematic illustration of setup for the (a) photocatalytic system and (b) photocatalytic reactor.

Toluene was introduced into the reactor with air controlled by an electronic mass flow controller (MFC). The gas was then circulated within the system for an hour until a steady state was reached. Once that was achieved, the UV lamp was turned on, and then photocatalytic oxidation started. The concentration of toluene throughout the reaction was measured using the GC/FID connected to the reactor, as shown in Figure S1a.

The photocatalytic reactor consists of two chambers with a total volume of 800 mL, separated by a stainless steel mash, where the photocatalytic filter was installed before each reaction (Figure S1b).

A gas inlet was located on the top compartment, and an outlet that was connected to the measurement instrument was positioned at the bottom part. The upper chamber was sealed with a borosilicate glass window. The temperature inside the reactor was kept at approximately 22 °C and the RH at 20%.

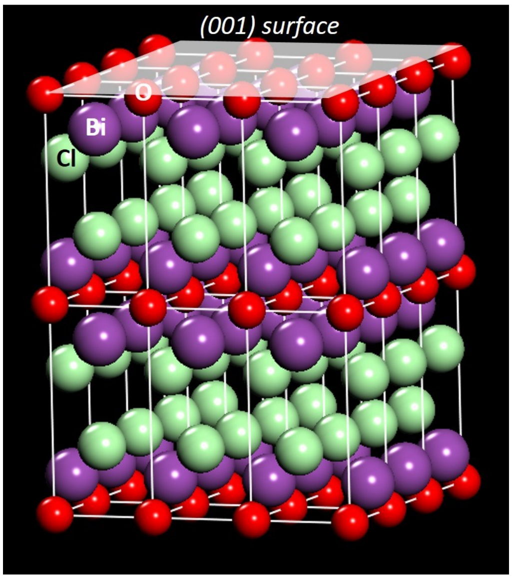

Figure S2. Crystal structure of the BiOCl(001) surface.

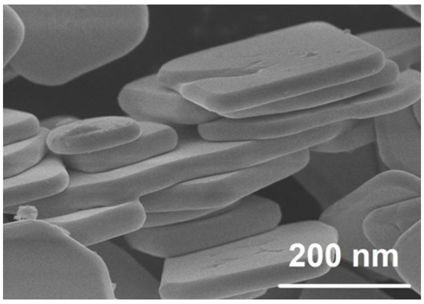

Figure S3. SEM image of the as-prepared P-BiOCl nanosheets.

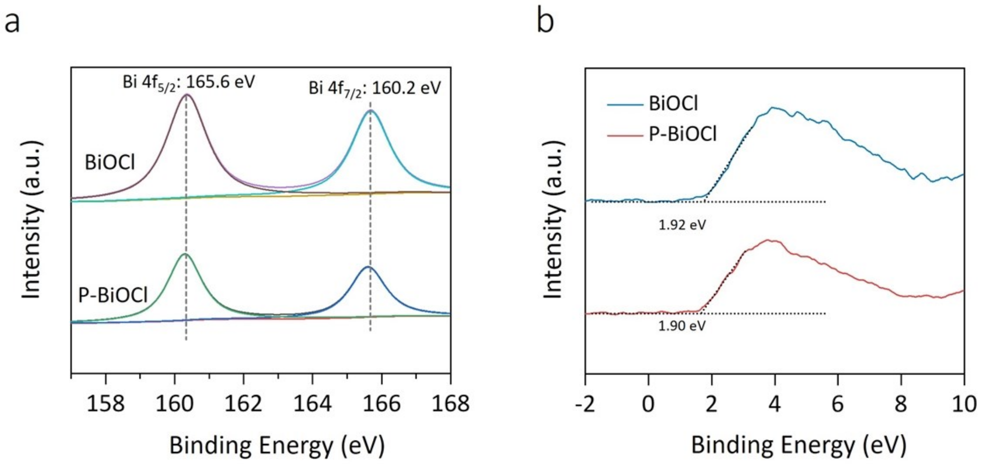

Figure S4. (a) High-resolution XPS spectra of Bi 4f regions and (b) XPS valence-band spectra of BiOCl and P-BiOCl.

High-resolution XPS spectra of Bi 4f peaks of BiOCl experienced no remarkable change after the adsorption of phosphoric acid (Figure S4a), ruling out the formation of Bi-P chemical bonds. Moreover, the XPS valence-band spectra of BiOCl and P-BiOCl shows that electronic structure in terms of the valence band position of BiOCl experienced no remarkable change after phosphoric adsorption (Figure S4b), suggesting the weak physical interactions between BiOCl and phosphoric acid.

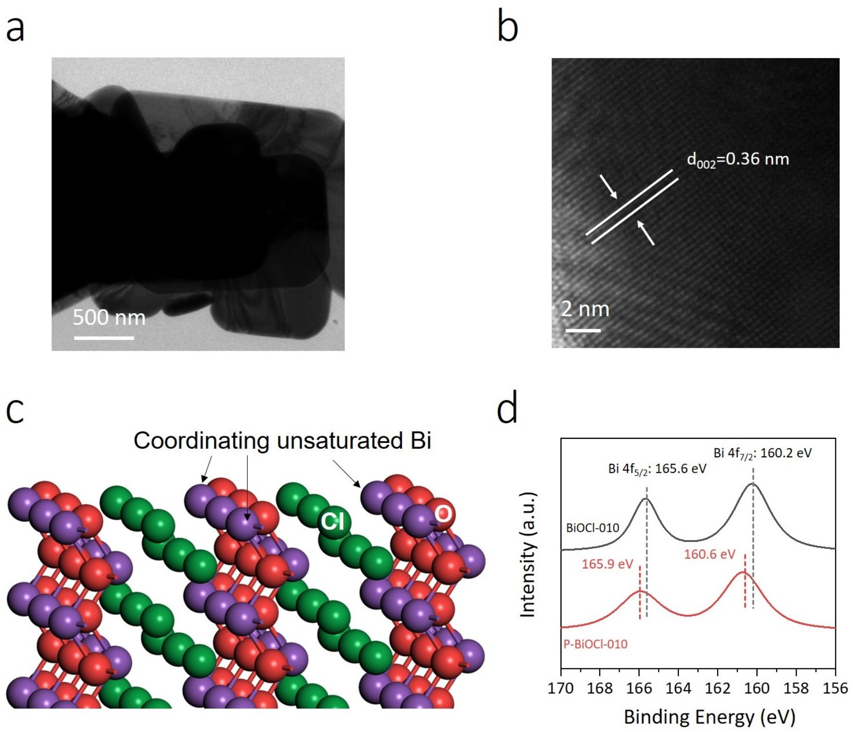

Figure S5. (a) TEM and (b) HRTEM images of BiOCl nanosheet with (010) surface exposed. (b) Surface structure of BiOCl(010) surface. (d) XPS spectra of BiOCl-010 after phosphoric acid adsorption (P-BiOCl-010).

For comparison, BiOCl nanosheets with typical (010) surface exposed (BiOCl-010) were prepared (Figure S5a). Such a surface could easily be prepared by pH adjustment during the hydrothermal process (Please see the Experimental Section for more details). According to high-resolution transmission electron microscopy, the clear (002) atomic plane with a lattice spacing of 0.36 nm revealed that the BiOCl nanosheet was (010) surface exposed (Figure S5a and 5b). Different from (001) surface, the (010) surface is exposed with coordinating unsaturated Bi atoms, which are not inclined to form a hydrogen bond with phosphoric acid, but rather chemical bonds (Figure S5c). As expected, the characteristic Bi $4f_{5/2}$ and Bi $4f_{7/2}$ binding energy peaks of BiOCl-010 were shifted toward higher binding energy after the adsorption of phosphoric acid, which prove the presence of strong chemical interaction between BiOCl-010 and $BiPO_4$.[1,2] Therefore, the reason why BiOCl(001) surface was specifically selected as the model was due to its closely-packed structure with exposed hydroxyl groups (Figure 1). This unusual surface structure ensures the multiple hydrogen bond (HB) interactions with phosphoric acid, which is a typical polyprotic acid of both HB-donor and HB-acceptor nature.

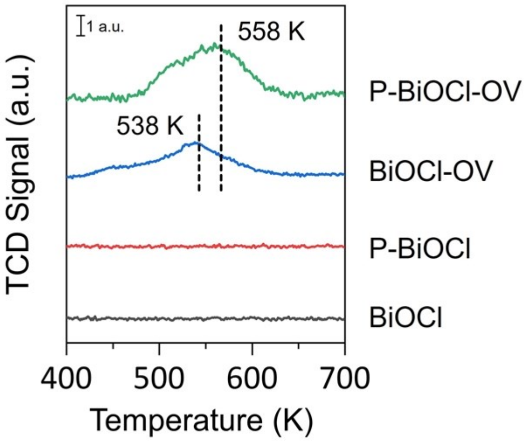

Figure S6. O_2-TPD profiles of the BiOCl photocatalysts with and without OVs.

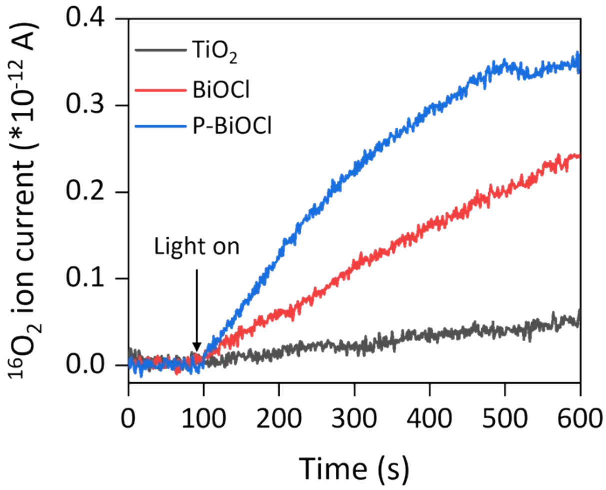

Figure S7. Time course for the generation of $^{16}O_2$ from BiOCl, P-BiOCl and TiO_2 under UV light irradiation detected via mass spectra.

Different from TiO_2, BiOCl can quickly generate OVs on the (001) surface under UV light under ambient conditions. This phenomenon is due to the rapid transfer and trapping of photoholes by surface O atoms.[3,4] First, the layered structure of BiOCl can accelerate the carriers' separation rate and facilitate the holes (h^+) trapping at the surface lattice O along the [001] direction under UV light. The holes trapped on the surface lattice O can partially neutralize the O anions through the $O^{2-} + h^+ \rightarrow O^-$ reaction, which is the first step for the OV formation. Second, the (001) surface of BiOCl is composed of crossed bridging rows with low-coordinated and closely interacted hydroxyl groups. The Bi–O bonds on the (001) facets are of long bond length and low energy and therefore favor the removal of the surface O atoms.[5,6] Such a surface structure is highly favorable for the OV generation by further trapping h^+ with two adjacent O anions $(O–O)^{4-}$ on the bridging rows via the $\underline{(O–O)^{4-} + 4h^+ \rightarrow O_2}$ reaction, releasing O_2 and leaving behind OVs on the surface. Simultaneously, photoelectrons were trapped on the OVs to achieve the overall charge balance, which partially oxidized Bi^{3+} ($\underline{Bi^{3+} + e^- \rightarrow Bi^{(3-x)+}}$). The released O_2 under UV light irradiation was *in situ* detected by mass spectrometry. The signal for O_2 (m/z 36) gradually increased for the BiOCl catalysts. In contrast, it was barely detected in the case of commercial TiO_2 (P25) (Figure S7). The much higher signal intensity for O_2 of P-BiOCl confirmed its higher tendency to generate OVs than BiOCl due to efficient trapping holes by surface O atoms.

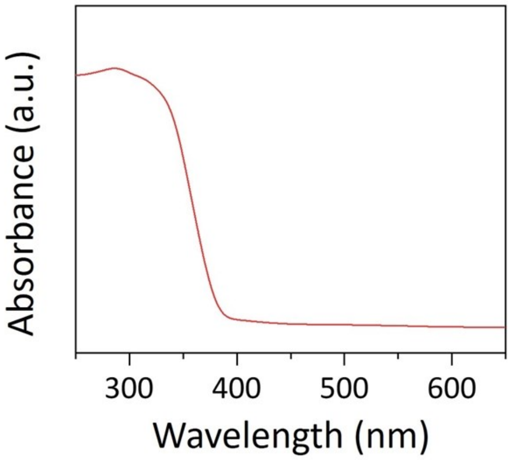

Figure S8. UV-vis absorption spectra of BiOCl.

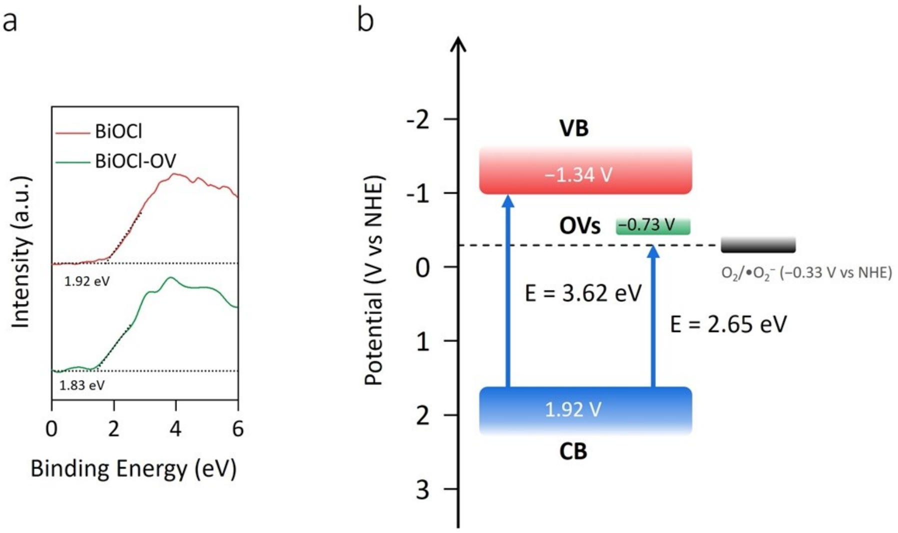

Figure S9. (a) XPS valence band spectra of the BiOCl with and without OVs. (b) Electronic energy-level diagram of BiOCl with OVs.

Based on the UV-vis absorption spectra and XPS valence band spectra, the bandgap of BiOCl and valence-band was determined to be around 3.26 eV and 1.92 eV, respectively. Valence band position of BiOCl experienced only a ~0.09 eV shift towards the conduction band after the introduction of

OVs (Figure S9a). This insignificant valence band shift is consistent with the fact that OVs mainly introduce localized electronic states beneath the conduction band without remarkably distorting the valence state of BiOCl. Thus, we schematically drew the band structure of BiOCl. The conduction band was determined to be −1.34 eV, which is much more negative than that of the standard redox potential of $O_2/{\bullet}O_2^-$ (−0.33 eV vs. NHE). According to previous results, the energy band corresponding to oxygen vacancies corresponded to a photoluminescence emission peak at 468 nm (2.65 eV).[5,6] Thus, the oxygen vacancy level was determined to be −0.73 eV, which is still capable of activating O_2 to superoxide radicals.

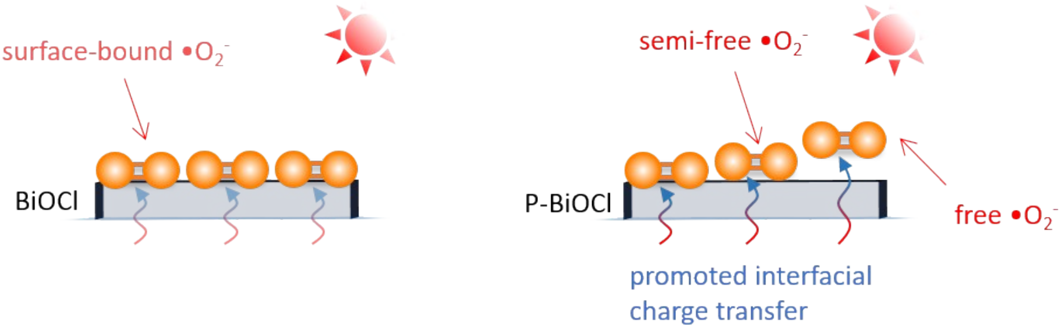

Figure S10. Schematic illustration of enhanced O_2 activation by promoted interfacial charge transfer.

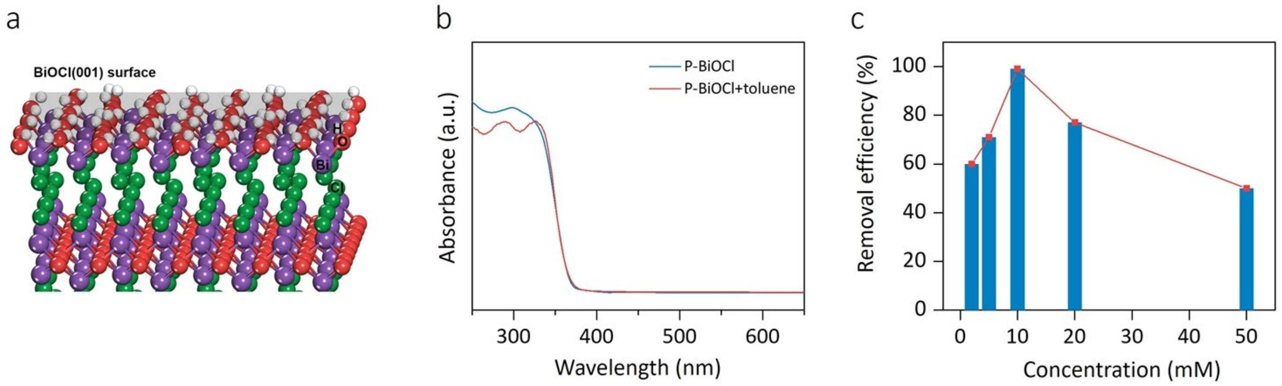

Figure S11. (a) Geometric structure of BiOCl(001) surface. (b) UV-vis absorption spectra of BiOCl and toluene-adsorbed BiOCl. (c) Influence of the concentration of phosphoric acid on photocatalytic performance of P-BiOCl.

The metal-to-ligand charge transfer was not a possible mechanism in our study. The BiOCl(001) surface is of a close-packed structure with exposure of high-density O atoms, ruling out the possible formation of surface metal complex compounds (Figure S11a). We also measured the UV-vis absorption spectra of P-BiOCl before and after the adsorption of toluene. Both the absorption intensity and edge of P-BiOCl experienced no remarkable change after the adsorption of toluene (Figure S11b). The best performance was observed for BiOCl treated with 10 mM H_3PO_4 (Figure S11c). If high concentration H_3PO_4 was added, adsorbed H_3PO_4 would block the active surface sites of BiOCl. Meanwhile, $BiPO_4$ impurities would be formed on BiOCl surface through anion exchange.

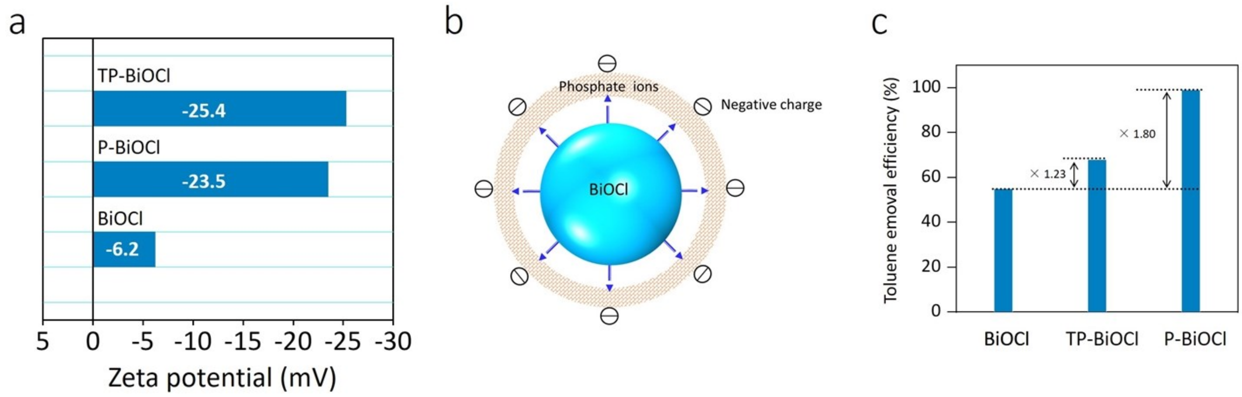

Figure S12. (a) Zeta potential of the as-prepared photocatalysts at pH 7 with the powder sample dispersing in water. (b) Schematic illustration of the surface negative charge formation. (c) Photocatalytic toluene removal efficiency on the as-prepared photocatalysts.

The zeta potential was employed to judge whether the surface charge had changed after the modification. As-prepared BiOCl was negatively-charged (−6.2 mV, pH = 7), consistent with the high-density oxygen atoms exposure characteristic of BiOCl(001) surface (Figure 1). As for P-BiOCl, its surface charge was −23.5 mV under the same conditions, suggesting the accumulation of more negative charges (Figure S12a-b). According to the previous results, the covering of the catalyst surface with negatively-charged phosphate anions could form a surface electrostatic field in the surface layer of photocatalysts.[7–9] Meanwhile, this surface electrostatic field can promote the separation of electron-hole pairs and suppress their recombination. To explore the influence of surface electrostatic field on photoreactivity of P-BiOCl for toluene oxidation, we adopted hydroxyl-free trisodium phosphate (Na_3PO_4) to functionalize BiOCl surface (TP-BiOCl). A similar surface charge change of BiOCl was observed after Na_3PO_4 adsorption, while a slight photoreactivity increase for toluene oxidation was observed (Figure S12c). Therefore, even phosphoric acid modification would lead to similar negative charge accumulation on the BiOCl surface and the possible formation of a surface electrostatic field, this effect was not the dominant factor for the observed remarkable photoreactivity increase of BiOCl.

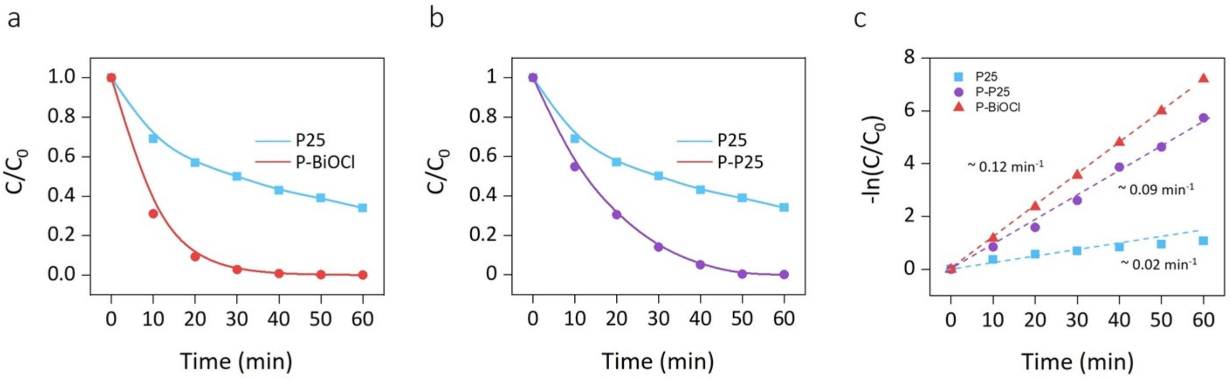

Figure S13. (a) Photocatalytic toluene oxidation over P-BiOCl and P25.

We prepared the phosphoric acid-modified Degussa P25 TiO_2 (P-P25) through the same method (Please see the Experimental Section for details). It is interesting to note that phosphoric acid modification also remarkably enhanced the photoreactivity of P25 (Figure S13b). However, P-BiOCl still exhibits faster toluene removal rate than P-P25 according to the corresponding pseudo-first-order rate constants (Figure S13c).

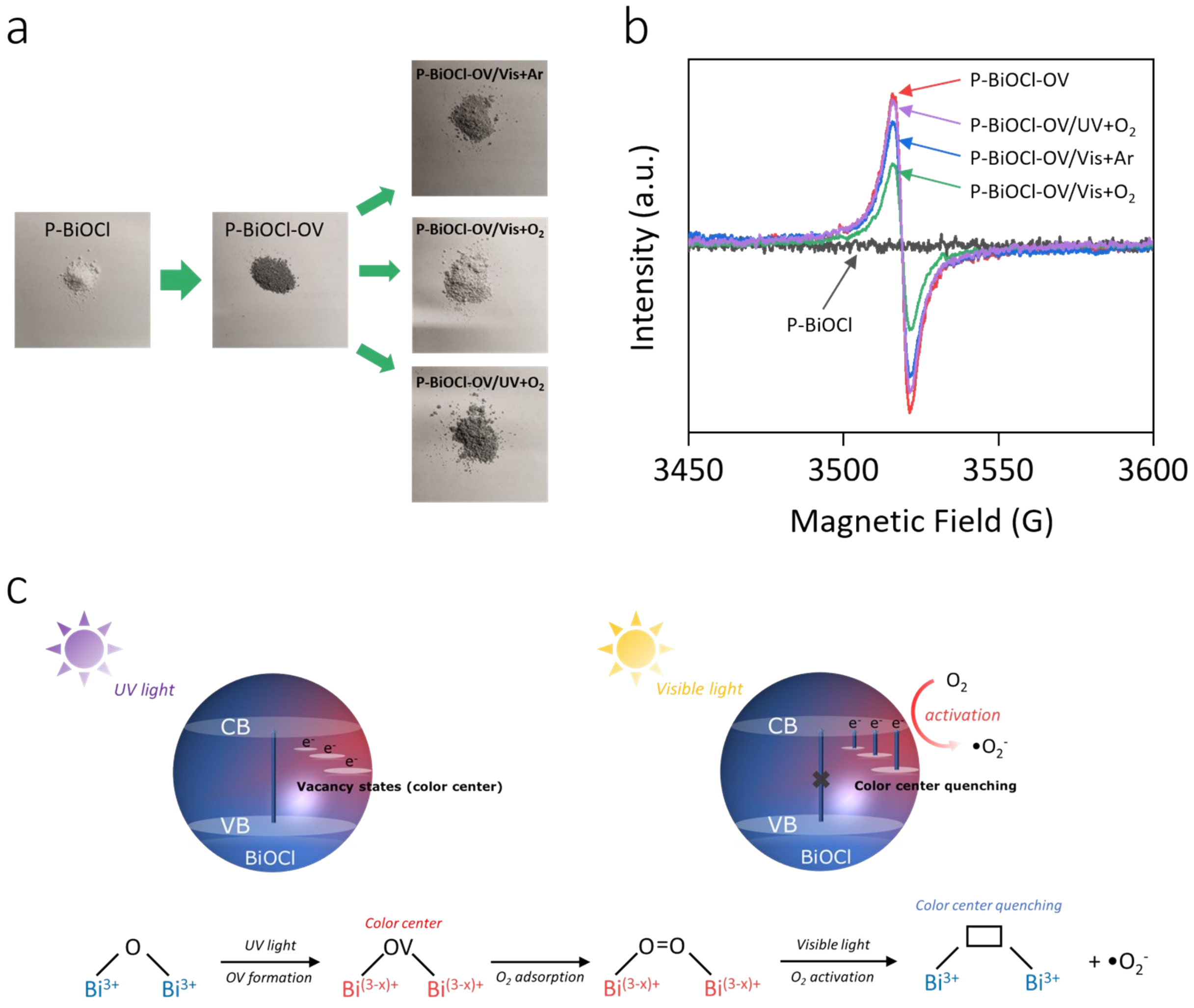

Figure S14. (a) Color change and (b) EPR spectra of the as-prepared photocatalyts. (c) Schematic illustration of the generation and quenching process of OVs.

The color change and OVs signal of P-BiOCl were investigated in different reaction atmospheres. In the Ar atmosphere, the color of P-BiOCl gradually changed from white to dark grey after one hour under UV light illumination, suggesting the formation of color centers due to the rapid loss of surface O atoms and generation of OVs (Figure S14a). The generation of OVs was further confirmed by the typical electron paramagnetic resonance (EPR) signal at $g = 2.001$ (Figure S14b). Under visible light (vis) irradiation, dark grey P-BiOCl-OV was slightly decolored after one hour of irradiation in the Ar atmosphere (Figure S14a and S14b). However, rapid decoloration was observed once O_2 was introduced along with the significant decrease of the EPR signal, suggesting the quenching of OVs (Figure S14a and S14b). The mechanism of color center quenching associated with both visible light and O_2 is similar to that of oxygen-deficient TiO_2 (Figure S14c).[10] Interestingly, dark grey P-BiOCl was not decolored under UV light irradiation, even in the presence of O_2. This result suggests quenched OVs were *in situ* regenerated under UV light, ensuring long term molecular oxygen activation, and can also explain the high stability of P-BiOCl for toluene removal.

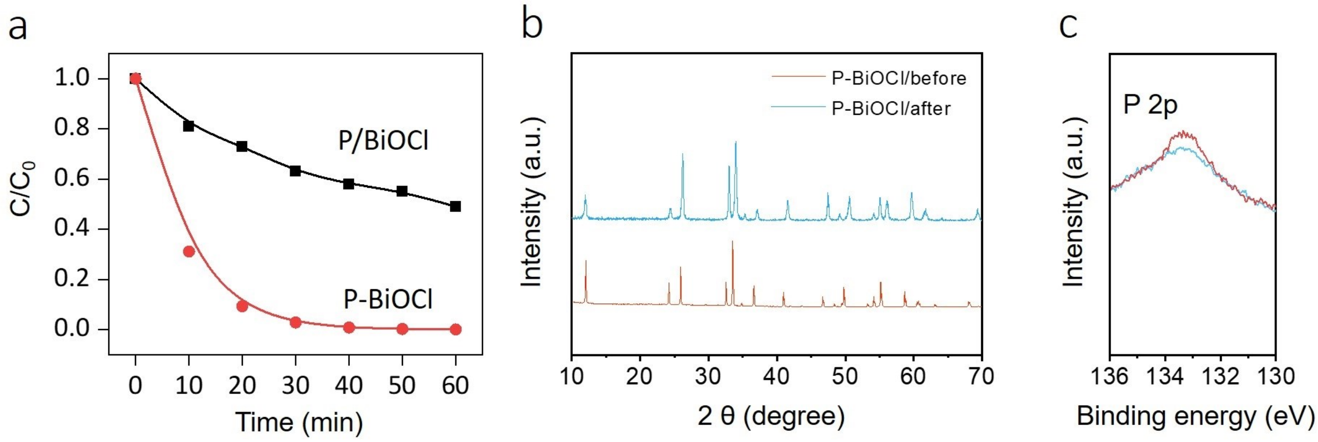

Figure S15. (a) Photocatalytic toluene oxidation over the as-prepared photocatalysts. (b) XRD pattern and (c) XPS spectra of the P-BiOCl before and after 5 cycles of photocatalytic toluene oxidation.

We physically mixed BiOCl and 1 wt% PA, which was denoted P/BiOCl. For photocatalytic NO oxidation, the efficiency of P/BiOCl was much weaker than that of P-BiOCl (Figure S15a). P-BiOCl maintained the same phase structure after five cycles of photocatalytic toluene oxidation (Figure S15a), suggesting the excellent photostability of P-BiOCl. P 2p binding energy located at 133.5 (±0.1) eV indicated that phosphorus in P-BiOCl was in a pentavalent-oxidation state (P^{5+}) and presented in the form of P-O bond (Figure S15b). After five cycles of photocatalytic toluene oxidation, both binding energy and intensity of the P 2p peak experienced no remarkable change, suggesting leaching of phosphoric acid was not a possible process in our case.

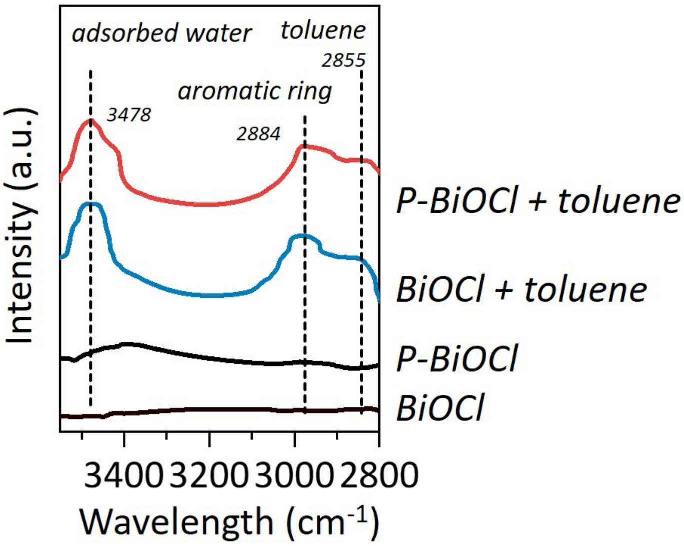

Figure S16. FTIR spectra of BiOCl and P-BiOCl after toluene adsorption in the dark.

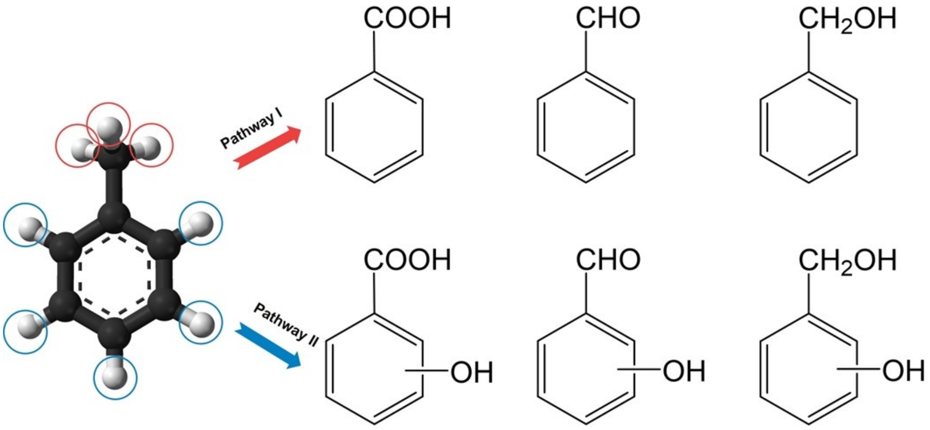

Figure S17. Schematic illustration of two pathways for H abstraction on toluene molecule.

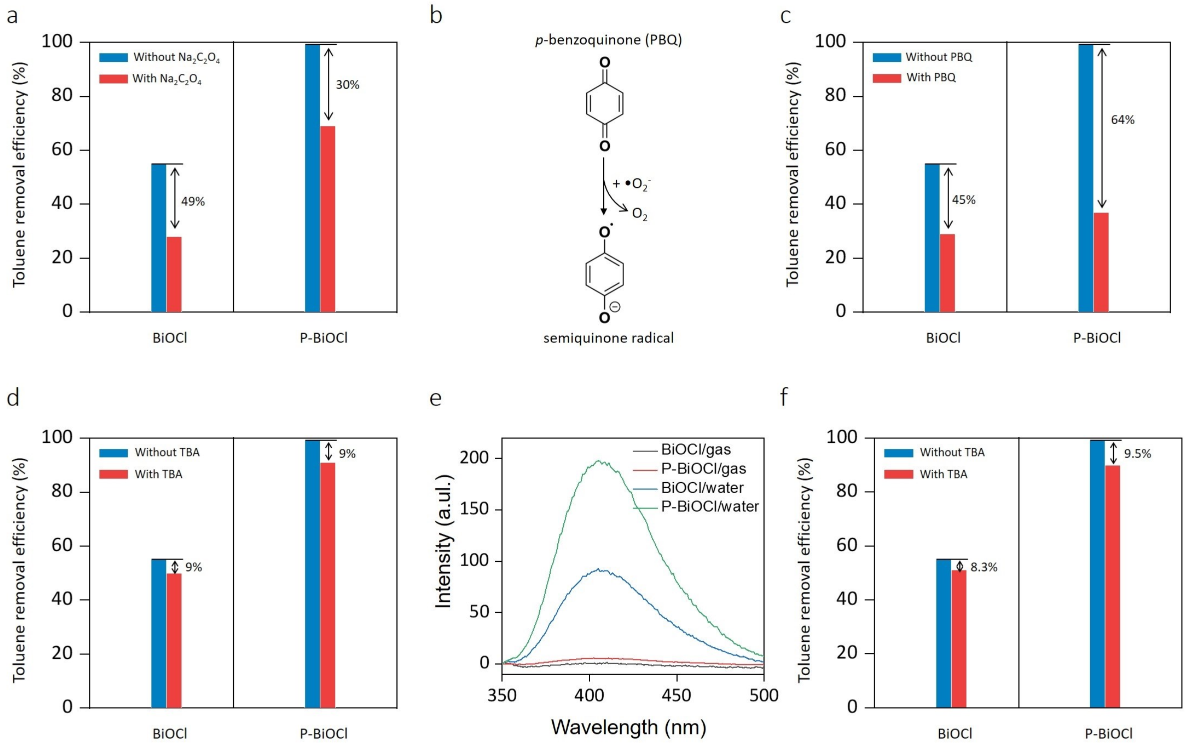

Figure S18. (a) Influence of $Na_2C_2O_4$ on photocatalytic toluene oxidation. (b) Schematic illustration of the *p*-benzoquinone-mediated •O_2^- quenching process. (c) Influence of *p*-benzoquinone on photocatalytic toluene oxidation. (d) Influence of TBA on photocatalytic toluene oxidation. (e) Fluorescence detection of the photogenerated H_2O_2 over the as-prepared BiOCl in the water and gas phase. (f) Influence of catalase on photocatalytic toluene oxidation.

The overall inhibition efficiency for photocatalytic toluene removal was estimated to be 49% and 30% for BiOCl and P-BiOCl, respectively, suggesting photoholes of BiOCl played a more critical role for toluene oxidation (Figure S18a). Figure S18b shows how •O_2^- is quenched by *p*-benzoquinone (PBQ). In this process, •O_2^- can quantitatively reduce *p*-benzoquinone to the semiquinone radical in aprotic media. For BiOCl, the inhibition efficiency was estimated to be 45% after the addition of 0.1 wt% PBQ (Figure S18c). As for P-BiOCl, the inhibition efficiency under the same condition was over 64%, suggesting •O_2^- played a pivotal role in oxidizing toluene (Figure S18c). For photocatalytic toluene oxidation in the gas phase, direct detection of H_2O_2 is not feasible. Thus, we tried to wash off the possibly formed H_2O_2 from the BiOCl surface after 60 min of light irradiation in the air and detected H_2O_2 through the fluorescence method. A (p-hydroxyphenyl) acetic acid (POHPAA) was used as the probe molecule. The reaction product of H_2O_2 with POHPAA fluorescence reagent had a strong fluorescent emission at 409 nm when excited at 315 nm.[11] For comparison, we detected the generation of H_2O_2 by BiOCl in the water phase. According to the fluorescence intensity, the generation of H_2O_2 was negligible in the gas phase compared with that in the water phase (Figure S18e). We also added catalase as the H_2O_2 scavenger ($2H_2O_2 \rightarrow 2H_2O + O_2$) and found that catalase did not remarkably influenced photoreactivity of BiOCl or P-BiOCl for toluene oxidation (Figure S18f). Thus, H_2O_2 was not the primary reactive species of BiOCl and P-BiOCl. Since H_2O_2 is usually associated with the protonation of reactive oxygen species ($\bullet O_2^- + e^- + 2H^+ \rightarrow H_2O_2$; $O_2^{2-} + 2H^+ \rightarrow H_2O_2$), the negligible formation of H_2O_2 in the gas phase was possibly due to low humidity during toluene oxidation in the gas phase. This is also the reason why superoxide radical ($\bullet OH$), which is derived from the oxidation of gaseous water by photoinduced holes ($H_2O + h^+ \rightarrow \bullet OH + H^+$), was also not a significant species in our system (Figure S18d).

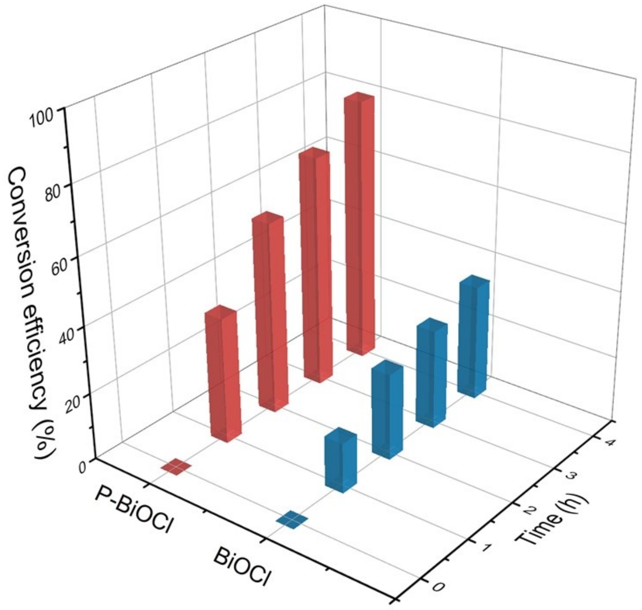

Figure S19. Photocatalytic benzaldehyde conversion on BiOCl and P-BiOCl.

For photocatalytic benzaldehyde oxidation in the aqueous phase, 20 mg of BiOCl or P-BiOCl was added into 3 ml of 1 mmol/L benzaldehyde solution with water as solvent under magnetic stirring condition. After the photocatalytic reaction, the photocatalysts were separated by centrifugation. The quantitative identification of benzaldehyde concentration in solution was performed through GC-MS. The conversion efficiency of benzaldehyde on P-BiOCl (80%) was over two times that of BiOCl (39%) after four hours of reaction (Figure S19).

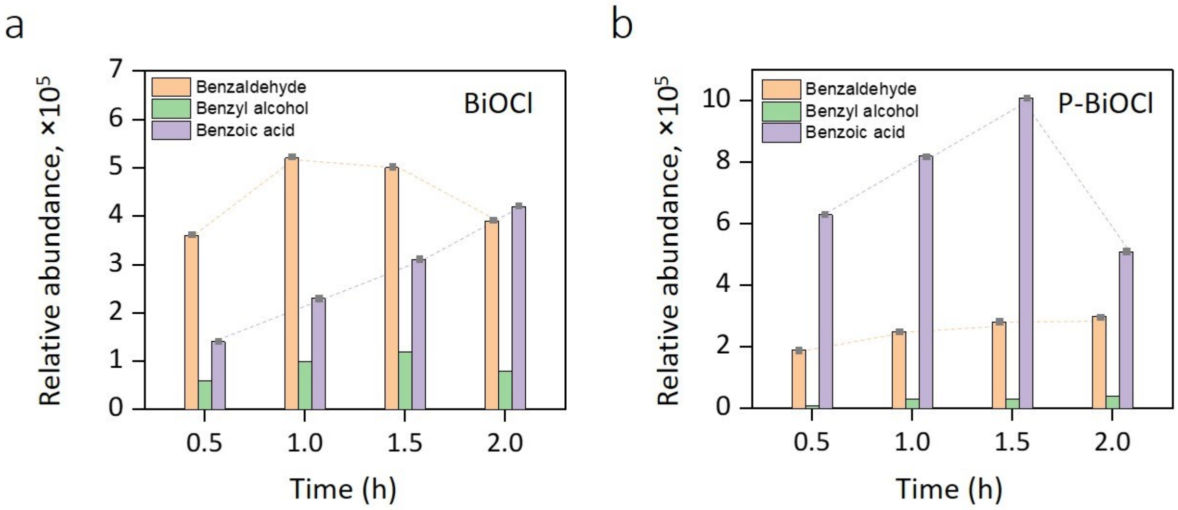

Figure S20. Temporal change in the concentrations of benzaldehyde, benzyl alcohol, and benzoic acid on BiOCl and P-BiOCl surfaces.

For BiOCl, surface benzaldehyde emerged as the major intermediates, whose concentration firstly increased and then decreased (Figure S20a). As for benzoic acid, it kept growing and becoming a significant intermediate (Figure S20a). For P-BiOCl, the major intermediate was benzoic acid, whose concentration was much higher than that of benzaldehyde and benzyl alcohol (Figure S20b). Different from BiOCl, both benzaldehyde benzyl alcohol maintained a relatively low concentration on the P-BiOCl surface (Figure S20b). A significant decrease of benzoic acid was observed after 1.5 h of photocatalytic reaction.

Table S1. Intermediates identified by GC-MS and LC-MS

No	Name	Structural formula	MS data (m/z)
1	Benzaldehyde	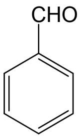	105
2	Benzoic acid	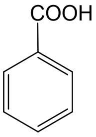	122
3	Benzyl alcohol	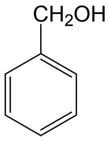	108
4	Benzene	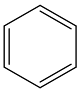	77
5	Succinic acid	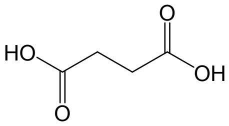	119
6	Butyraldehyde	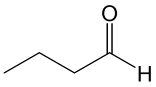	71
7	Pyruvic acid	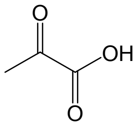	87
8	Propionic acid	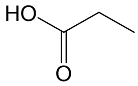	73
9	Acetic acid	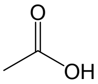	59
10	Acetaldehyde	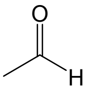	44

11	Formic acid	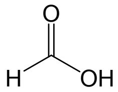	45

Table S2. Intermediates and their relative abundance identified by GC–MS under different conditions

Intermediates	Relative abundance, ×10^5			
	BiOCl		P-BiOCl	
	Without $Na_2C_2O_4$	With $Na_2C_2O_4$	Without $Na_2C_2O_4$	With $Na_2C_2O_4$
Benzaldehyde	5.2	2.1	2.5	1.3
Benzyl alcohol	1.0	0.4	0.3	0.1
Benzoic acid	2.3	1.6	**8.2**	**6.5**

References

1 F. Duo, Y. Wang, X. Mao, X. Zhang, Y. Wang and C. Fan, *Appl. Surf. Sci.*, 2015, **340**, 35–42.

2 X. Gao, G. Tang, W. Peng, Q. Guo and Y. Luo, *Chem. Eng. J.*, 2019, **360**, 1320–1329.

3 J. Jiang, K. Zhao, X. Xiao and L. Zhang, *J. Am. Chem. Soc.*, 2012, **134**, 4473–4476.

4 K. Zhao, L. Zhang, J. Wang, Q. Li, W. He and J. J. Yin, *J. Am. Chem. Soc.*, 2013, **135**, 15750–15753.

5 X. Shen, G. Dong, L. Wang, L. Ye and J. Sun, *Adv. Mater. Interfaces*, 2019, **6**, 1901032.

6 L. Ye, K. Deng, F. Xu, L. Tian, T. Peng and L. Zan, *Phys. Chem. Chem. Phys.*, 2012, **14**, 82–85.

7 D. Zhao, C. Chen, Y. Wang, H. Ji, W. Ma, L. Zang and J. Zhao, *J. Phys. Chem. C*, 2008, **112**, 5993–6001.

8 F. Chen, J. Zhao and H. Hidaka, *Res. Chem. Intermed.*, 2003, **29**, 733–748.

9 M. Xie, J. Bian, M. Humayun, Y. Qu, Y. Feng and L. Jing, *Chem. Commun.*, 2015, **51**, 2821–2823.

10 M. Xing, J. Zhang, F. Chen and B. Tian, *Chem. Commun.*, 2011, **47**, 4947.

11\. Lazrus, A. L.; Kok, G. L.; Gitlin, S. N.; Lind, J. A.; McLaren, S. E. *Anal. Chem.* **1985**, *57*, 917–922.